Semicond. Sci. Technol. **15** (2000) R13–R27. Printed in the UK PII: S0268-1242(00)05774-6

TOPICAL REVIEW

Theory of transport in carbon nanotubes

Tsuneya Ando

Institute for Solid State Physics, University of Tokyo, 7–22–1 Roppongi, Minato-ku, Tokyo 106-8666, Japan

Received 1 September 1999, accepted for publication 17 February 2000

Abstract. A brief review is given of electronic and transport properties of carbon nanotubes mainly from a theoretical point of view. The topics include a giant Aharonov–Bohm effect on the bandgap and a Landau-level formation in magnetic fields, absence of backward scattering except for scatterers with a potential range smaller than the lattice constant, a conductance quantization in the presence of short-range and strong scatterers such as lattice vacancies and transport across junctions between nanotubes with different diameters.

1. Introduction

Graphite needles called carbon nanotubes (CNs) were discovered recently [1, 2] and have been a subject of an extensive study. A CN is a few concentric tubes of two-dimensional (2D) graphite consisting of carbon-atom hexagons arranged in a helical fashion about the axis. The diameter of CNs is usually between 20 and 300 Å and their length can exceed 1 μm. The distance between adjacent sheets or walls is larger than the distance between nearest neighbour atoms in a graphite sheet and therefore electronic properties of CNs are dominated by those of a single layer CN. Single-wall nanotubes are produced in the form of ropes [3, 4]. The purpose of this paper is to give a brief review of recent theoretical study on transport properties of carbon nanotubes.

Figure 1 shows a transmission micrograph image of multi-wall nanotubes and figure 2 a computer graphic image of a single-wall nanotube. Carbon nanotubes can be either a metal or semiconductor, depending on their diameters and helical arrangement. The condition of whether a CN is metallic or semiconducting can be obtained based on the band structure of a 2D graphite sheet and periodic boundary conditions along the circumference direction. This result was first predicted by means of a tight-binding model ignoring the effect of the tube curvature [5–14].

These properties can be well reproduced in a $\boldsymbol{k} \cdot \boldsymbol{p}$ method or an effective-mass approximation [15]. In fact, the effective-mass scheme has been used successfully in the study of wide varieties of electronic properties of CN. Some examples are magnetic properties [16] including the Aharonov–Bohm effect on the bandgap [15], optical absorption spectra [17, 18], exciton effects [19], lattice instabilities in the absence [20] and presence of a magnetic field [21, 22], and magnetic properties of ensembles of nanotubes [23].

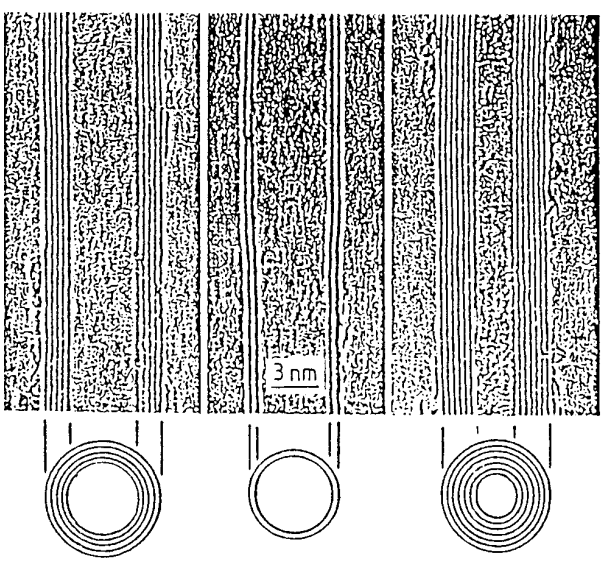

Figure 1. Some examples of transmission micrograph images of carbon nanotubes [1]. The diameter is 67, 55, and 65 Å from left to right.

Transport properties of CNs are interesting because of their unique topological structure. There have been some reports on experimental study of transport in CN bundles [24] and ropes [25, 26]. Transport measurements became possible for a single multi-wall nanotube [27–32] and a single single-wall nanotube [33–37]. Single-wall nanotubes usually exhibit large charging effects presumably due to nonideal contacts.

 © 2000 IOP Publishing Ltd

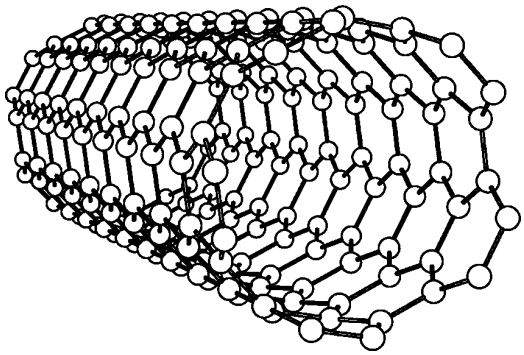

Figure 2. A computer graphic image of a single-wall armchair nanotube.

In this paper we shall mainly discuss transport properties of nanotubes obtained theoretically in the $\boldsymbol{k}\cdot\boldsymbol{p}$ method combined with a tight-binding model. In section 2 the effective-mass equation is introduced and the band structure is discussed with a special emphasis on Aharonov–Bohm effects and formation of Landau levels in magnetic fields. Effects of impurity scattering are discussed and the total absence of backward scattering is pointed out except for scatterers with a potential range smaller than the lattice constant in section 3. The conductance quantization in the presence of lattice vacancies, i.e., strong and short-range scatterers, is discussed in section 4. In section 5 the transport across a junction of nanotubes with different diameters through a pair of topological defects such as five- and seven-member rings is discussed. It is worth mentioning that several papers giving general reviews of electronic properties of nanotubes have been published already [38–42].

2. Energy bands and Aharonov–Bohm effect

Figure 3 shows the lattice structure and the first Brillouin zone of 2D graphite together with the coordinate systems of a nanotube. The unit cell of the 2D graphite has an area $\sqrt{3}a^2/2$ and contains two carbon atoms (denoted as A and B). A nanotube is specified by a chiral vector $\boldsymbol{L} = n_a\boldsymbol{a} + n_b\boldsymbol{b}$ with integer n_a and n_b and basis vectors $\boldsymbol{a}$ and $\boldsymbol{b}$ ($|\boldsymbol{a}| = |\boldsymbol{b}| = a = 2.46$ Å). In the coordinate system fixed onto a graphite sheet, we have $\boldsymbol{a} = (a, 0)$ and $\boldsymbol{b} = (-a/2, \sqrt{3}a/2)$. For convenience we introduce another coordinate system where the x direction is along the circumference $\boldsymbol{L}$ and the y direction is along the axis of CN. The direction of $\boldsymbol{L}$ is denoted by the chiral angle η.

A graphite sheet is a zero-gap semiconductor in the sense that the conduction and valence bands consisting of π states cross at K and K′ points of the Brillouin zone, whose wave vectors are given by $\boldsymbol{K} = (2\pi/a)(1/3, 1/\sqrt{3})$ and $\boldsymbol{K}' = (2\pi/a)(2/3, 0)$, as shown in figure 4 [43]. The K and K′ points are not equivalent because they are not connected by reciprocal lattice vectors.

Electronic states near a K point of 2D graphite are described by the $\boldsymbol{k}\cdot\boldsymbol{p}$ equation [15, 44]:

$$\gamma(\sigma_x\hat{k}_x + \sigma_y\hat{k}_y)\boldsymbol{F}_K(\boldsymbol{r}) = \gamma(\boldsymbol{\sigma}\cdot\hat{\boldsymbol{k}})\boldsymbol{F}^K(\boldsymbol{r}) = \varepsilon\boldsymbol{F}^K(\boldsymbol{r}) \quad (2.1)$$

where γ is the band parameter, $\hat{\boldsymbol{k}} = (\hat{k}_x, \hat{k}_y)$ is a wave-vector operator, ε is the energy, and σ_x, σ_y and σ_z are the Pauli spin matrices. In the above equations, the envelope functions are written as

$$\boldsymbol{F}^K(\boldsymbol{r}) = \begin{pmatrix} F_A^K(\boldsymbol{r}) \\ F_B^K(\boldsymbol{r}) \end{pmatrix}. \quad (2.2)$$

Equation (2.1) has the form of Weyl's equation for neutrinos (a Dirac electron with a vanishing rest mass).

For nanotubes with a sufficiently large diameter, their electronic states near the Fermi level can be obtained by imposing the periodic boundary condition in the circumference direction, $\Psi(\boldsymbol{r} + \boldsymbol{L}) = \Psi(\boldsymbol{r})$. The Bloch functions at a K point change their phase by $\exp(\mathrm{i}\boldsymbol{K}\cdot\boldsymbol{L}) = \exp(2\pi\mathrm{i}\nu/3)$, where ν is an integer defined by $n_a + n_b = 3M + \nu$ with integer M and can take 0 and ±1. Because $\Psi(\boldsymbol{r})$ is written as a product of the Bloch function and the envelope function, this phase change should be canceled by that of the envelope functions and the boundary conditions for the envelope functions are given by

$$\boldsymbol{F}^K(\boldsymbol{r} + \boldsymbol{L}) = \boldsymbol{F}^K(\boldsymbol{r})\exp\left(-\frac{2\pi\mathrm{i}\nu}{3}\right). \quad (2.3)$$

Energy levels in CN for the K point are obtained by putting $k_x = \kappa_\nu(n)$ with

$$\kappa_\nu(n) = \frac{2\pi}{L}\left(n - \frac{\nu}{3}\right) \quad (2.4)$$

and $k_y = k$ in the above $\boldsymbol{k}\cdot\boldsymbol{p}$ equation as [15]

$$\varepsilon_\nu^{(\pm)}(n, k) = \pm\gamma\sqrt{\kappa_\nu(n)^2 + k^2} \quad (2.5)$$

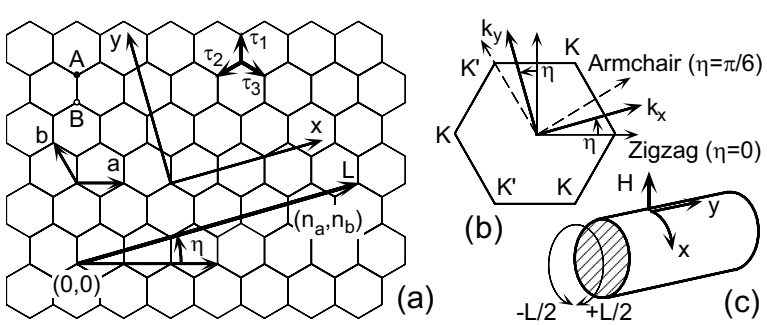

Figure 3. (a) Lattice structure of two-dimensional graphite sheet. η is the chiral angle. The coordinates are chosen in such a way that x is along the circumference of a nanotube and y is along the axis. (b) The first Brillouin zone and K and K′ points. (c) The coordinates for a nanotube.

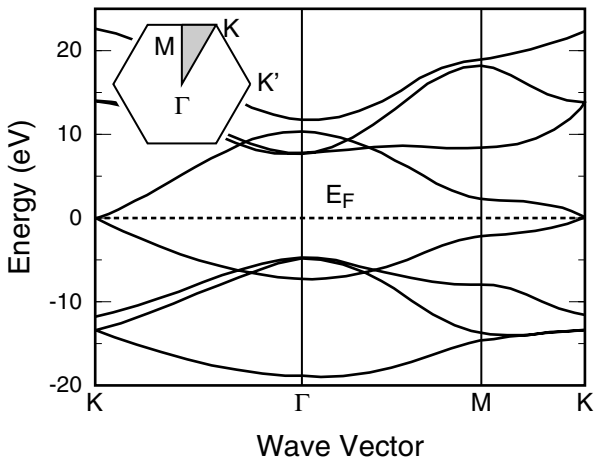

Figure 4. Energy gap versus magnetic flux passing through the tube cross section for metallic ($\nu = 0$) and semiconducting ($\nu = \pm 1$) CN.

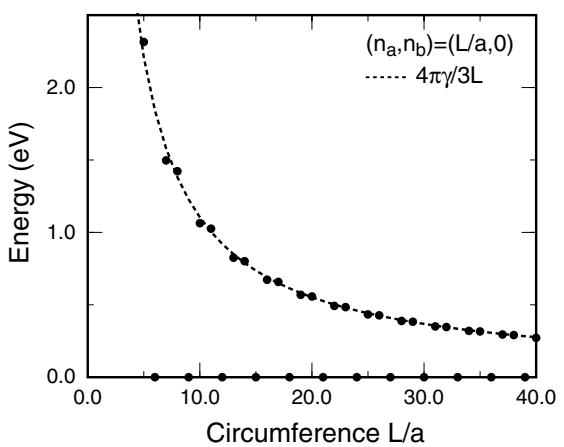

Figure 5. The bandgap of a zigzag nanotube as a function of the circumference L/a. The dots represent tight-binding results and the dotted line the result of the lowest-order $\boldsymbol{k}\cdot\boldsymbol{p}$ scheme.

where $L = |\boldsymbol{L}|$, n is an integer, and the upper (+) and lower (−) signs represent the conduction and valence bands, respectively. Those for the K′ point are obtained by replacing ν by $-\nu$ in the above equations. This shows that CN becomes metallic for $\nu = 0$ and semiconducting with gap $E_g = 4\pi\gamma/3L$ for $\nu = \pm 1$. Figure 5 compares this gap to that obtained in a tight-binding model.

In the presence of a magnetic field, the wave-vector operators become $\hat{\boldsymbol{k}} = -\mathrm{i}\boldsymbol{\nabla} + (e\boldsymbol{A}/c\hbar)$, where $\boldsymbol{A} = (A_x, A_y)$ is the vector potential. When the field is parallel to the axis, i.e., in the presence of a magnetic flux ϕ passing through the cross section, this leads to the change in the boundary condition $\Psi(\boldsymbol{r} + \boldsymbol{L}) = \Psi(\boldsymbol{r})\exp(2\pi\mathrm{i}\varphi)$ with $\varphi = \phi/\phi_0$, where $\phi_0 = ch/e$ is the magnetic flux quantum. Consequently, $\kappa_\nu(n)$ is replaced by $\kappa_{\nu\varphi}(n)$ with

$$\kappa_{\nu\varphi}(n) = \frac{2\pi}{L}\left(n + \varphi - \frac{\nu}{3}\right). \tag{2.6}$$

The corresponding result for the K′ point is again obtained by the replacement $\nu \to -\nu$. The bandgap exhibits an

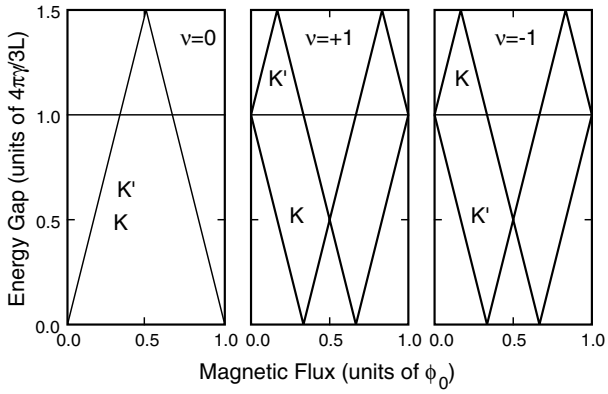

Figure 6. Energy gap versus magnetic flux passing through the tube cross section for metallic ($\nu = 0$) and semiconducting ($\nu = \pm 1$) CN. After [15].

oscillation between 0 and $2\pi\gamma/L$ with period ϕ_0 as shown in figure 6. This giant Aharonov–Bohm (AB) effect on the bandgap is a unique property of CNs. The AB effect appears also in a tunnelling conductance across a finite-length CN [45].

In the presence of a magnetic field H perpendicular to the tube axis, we can use the gauge

$$\boldsymbol{A} = \left(0, \frac{LH}{2\pi}\sin\frac{2\pi x}{L}\right) \tag{2.7}$$

and the effective field for electrons in a CN is given by the component perpendicular to the surface, i.e., $H(x) = H\cos(2\pi x/L)$. The parameter characterizing its strength is given by $\alpha = (L/2\pi l)^2$, where $l = \sqrt{c\hbar/eH}$ is the magnetic length or the radius of the smallest cyclotron orbit. In the case $(L/2\pi l)^2 \ll 1$, the field can be regarded as a small perturbation, while in the case $(L/2\pi l)^2 \gg 1$, Landau levels are formed on the cylinder surface. An interesting feature of Weyl's equation lies in the fact that Landau levels are formed at energy $\varepsilon = 0$ independent of the field strength. This anomaly has long been known as the origin of a large diamagnetism of graphite [46, 47].

Consider a metallic nanotube for example. The energy levels and wavefunctions are analytically obtained for $\varepsilon \sim 0$ in this case [48]. The results are

$$\boldsymbol{F}^K_{sk} = \frac{1}{\sqrt{2A}}\begin{pmatrix} -\mathrm{i}s(k/|k|)F_-(x) \\ F_+(x)\end{pmatrix}\exp(\mathrm{i}ky)$$

$$\boldsymbol{F}^{K'}_{sk} = \frac{1}{\sqrt{2A}}\begin{pmatrix} +\mathrm{i}s(k/|k|)F_+(x) \\ F_-(x)\end{pmatrix}\exp(\mathrm{i}ky) \tag{2.8}$$

with

$$F_\pm(x) = \frac{1}{\sqrt{LI_0(2\alpha)}}\exp\left(\pm\alpha\cos\frac{2\pi x}{L}\right) \tag{2.9}$$

where A is the length of the nanotube, $s = +1$ and -1 for the conduction and valence band, respectively, and $I_0(z)$ is the modified Bessel function of the first kind defined as

$$I_0(z) = \int_0^\pi \frac{\mathrm{d}\theta}{\pi}\exp(z\cos\theta). \tag{2.10}$$

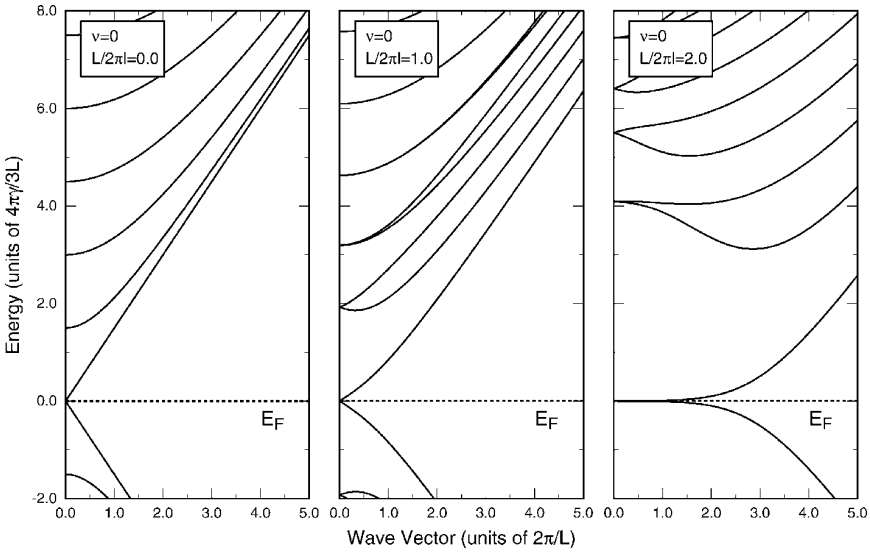

Figure 7. Some examples of calculated energy bands of a metallic CN in magnetic fields perpendicular to the axis.

In high magnetic fields ($\alpha \gg 1$), $\boldsymbol{F}_-$ is localized around $x = \pm L/2$, i.e., at the bottom side of the cylinder and $\boldsymbol{F}_+$ is localized around the top side $x = 0$. The corresponding eigenenergies are given by

$$\varepsilon_s(k) = \frac{s\gamma|k|}{I_0(2\alpha)} \tag{2.11}$$

which gives the group velocity

$$v = \frac{\gamma}{\hbar I_0(2\alpha)} \tag{2.12}$$

and the density of states

$$D(0) = \frac{I_0(2\alpha)}{\pi\gamma} \tag{2.13}$$

at $\varepsilon = 0$. We should note that

$$I_0(2\alpha) \approx \begin{cases} 1 + \alpha^2 + \cdots & (\alpha \ll 1) \\ \mathrm{e}^{2\alpha}/\sqrt{4\pi\alpha} & (\alpha \gg 1). \end{cases} \tag{2.14}$$

This means that the group velocity for states at $\varepsilon = 0$ decreases and consequently the density of states increases exponentially with the increase of the magnetic field in the high-field regime.

Figure 7 gives some examples of energy bands of a metallic CN in perpendicular magnetic fields [15], which clearly show the formation of flat Landau levels at the Fermi level in high fields. It is worth mentioning that there is no difference in the spectra between metallic and semiconducting CNs and in the presence and absence of an AB flux for $(L/2\pi l)^2 \gg 1$, because the wave function is localized in the circumference direction and the boundary condition becomes irrelevant.

Table 1 shows some examples of actual magnetic-field strength corresponding to the conditions $(L/2\pi l)^2 = 1$ and $\phi/\phi_0 = 1$ as a function of the circumference and the radius. For a typical single-wall armchair nanotube having circumference $L = \sqrt{3}ma$ with $m = 10$, the required magnetic field is too large, but can be easily accessible by using a pulse magnet for typical multi-wall nanotubes with a diameter ∼50 Å.

Table 1. Some examples of actual magnetic-field strength corresponding to the conditions $(L/2\pi l)^2 = 1$ and $\phi/\phi_0 = 1$ as a function of the circumference and the radius. The bandgap of a semiconducting nanotube is also shown ($\gamma = 6.46$ eV Å).

Circumference (Å)	50	100	200	400	800
Diameter (Å)	16	32	64	127	255
Gap (meV)	541	270	135	68	34
Magnetic ϕ_0	2080	520	130	32	8
field (T) $(L/2\pi l)^2 = 1$	1040	260	65	16	4

For nanotubes with a small circumference, we have to consider higher-order $\boldsymbol{k} \cdot \boldsymbol{p}$ terms in the Hamiltonian. A higher-order $\boldsymbol{k} \cdot \boldsymbol{p}$ equation was derived in a simple tight-binding model including only a π orbital for each carbon atom as [49]

$$\begin{pmatrix} 0 & & \\ \gamma\left[(\hat{k}_x + \mathrm{i}\hat{k}_y) + \dfrac{a\,\mathrm{e}^{-3\mathrm{i}\eta}}{4\sqrt{3}}(\hat{k}_x - \mathrm{i}\hat{k}_y)^2\right] & & \\ & \gamma\left[(\hat{k}_x - \mathrm{i}\hat{k}_y) + \dfrac{a\,\mathrm{e}^{3\mathrm{i}\eta}}{4\sqrt{3}}(\hat{k}_x + \mathrm{i}\hat{k}_y)^2\right] & \\ & & 0 \end{pmatrix} \boldsymbol{F}^K = \varepsilon \boldsymbol{F}^K \tag{2.15}$$

for the K point, where η is the chiral angle. This gives trigonal warping of the band around the K point in 2D graphite and gives a small correction to the bandgap of the CN. As shown in figure 8, the correction takes account of the deviation from the tight-binding result present in the lowest-order $\boldsymbol{k} \cdot \boldsymbol{p}$ theory almost completely. In the presence of a magnetic field perpendicular to the axis, the higher-order term was shown to cause the appearance of a small bandgap except in armchair nanotubes and a shift of the wave vector corresponding to $\varepsilon = 0$ in armchair nanotubes [49].

3. Absence of backward scattering

In the presence of impurities, electronic states in the vicinity of K and K′ points can be mixed with each other. Therefore, we should use a 4×4 Schrödinger equation

$$\mathcal{H}\boldsymbol{F} = \varepsilon \boldsymbol{F} \tag{3.1}$$

with

$$\boldsymbol{F} = \begin{pmatrix} \boldsymbol{F}^{K} \\ \boldsymbol{F}^{\mathrm{K}'} \end{pmatrix} \qquad \boldsymbol{F}^{\mathrm{K}'} = \begin{pmatrix} F_A^{\mathrm{K}'} \\ F_B^{\mathrm{K}'} \end{pmatrix} \tag{3.2}$$

and

$$\mathcal{H} = \mathcal{H}_0 + V. \tag{3.3}$$

The unperturbed Hamiltonian is given by

$$\mathcal{H}_0 = \gamma \begin{pmatrix} 0 & \hat{k}_x - \mathrm{i}\hat{k}_y & 0 & 0 \\ \hat{k}_x + \mathrm{i}\hat{k}_y & 0 & 0 & 0 \\ 0 & 0 & 0 & \hat{k}_x + \mathrm{i}\hat{k}_y \\ 0 & 0 & \hat{k}_x - \mathrm{i}\hat{k}_y & 0 \end{pmatrix}. \tag{3.4}$$

The effective potential of an impurity is written as [50]

$$V = \begin{pmatrix} u_A(\boldsymbol{r}) & 0 & \mathrm{e}^{\mathrm{i}\eta}u'_A(\boldsymbol{r}) & 0 \\ 0 & u_B(\boldsymbol{r}) & 0 & -\omega^{-1}\mathrm{e}^{-\mathrm{i}\eta}u'_B(\boldsymbol{r}) \\ \mathrm{e}^{-\mathrm{i}\eta}u'_A(\boldsymbol{r})^* & 0 & u_A(\boldsymbol{r}) & 0 \\ 0 & -\omega\,\mathrm{e}^{\mathrm{i}\eta}u'_B(\boldsymbol{r})^* & 0 & u_B(\boldsymbol{r}) \end{pmatrix} \tag{3.5}$$

where $\omega = \exp(2\pi\mathrm{i}/3)$. If we use a tight-binding model, we obtain the explicit expressions for the potentials as

$$\begin{aligned} u_A(\boldsymbol{r}) &= \sum_{\boldsymbol{R}_A} g(\boldsymbol{r}-\boldsymbol{R}_A)u_A(\boldsymbol{R}_A) \\ u_B(\boldsymbol{r}) &= \sum_{\boldsymbol{R}_B} g(\boldsymbol{r}-\boldsymbol{R}_B)u_B(\boldsymbol{R}_B) \\ u'_A(\boldsymbol{r}) &= \sum_{\boldsymbol{R}_A} g(\boldsymbol{r}-\boldsymbol{R}_A)\,\mathrm{e}^{\mathrm{i}(\boldsymbol{K}'-\boldsymbol{K})\cdot\boldsymbol{R}_A}u_A(\boldsymbol{R}_A) \\ u'_B(\boldsymbol{r}) &= \sum_{\boldsymbol{R}_B} g(\boldsymbol{r}-\boldsymbol{R}_B)\,\mathrm{e}^{\mathrm{i}(\boldsymbol{K}'-\boldsymbol{K})\cdot\boldsymbol{R}_B}u_B(\boldsymbol{R}_B) \end{aligned} \tag{3.6}$$

where $u_A(\boldsymbol{R}_A)$ and $u_B(\boldsymbol{R}_B)$ are the local site energy at site $\boldsymbol{R}_A$ and $\boldsymbol{R}_B$, respectively, due to the impurity potential and $g(\boldsymbol{r})$ is a smoothing function having a range of the order of the lattice constant a and satisfying the normalization condition

$$\sum_{\boldsymbol{R}_A} g(\boldsymbol{r}-\boldsymbol{R}_A) = \sum_{\boldsymbol{R}_B} g(\boldsymbol{r}-\boldsymbol{R}_B) = 1. \tag{3.7}$$

When the potential range is much shorter than the circumference L, we have

$$\begin{aligned} u_A(\boldsymbol{r}) &= u_A\delta(\boldsymbol{r}-\boldsymbol{r}_A) \\ u_B(\boldsymbol{r}) &= u_B\delta(\boldsymbol{r}-\boldsymbol{r}_B) \\ u'_A(\boldsymbol{r}) &= u'_A\delta(\boldsymbol{r}-\boldsymbol{r}_A) \\ u'_B(\boldsymbol{r}) &= u'_B\delta(\boldsymbol{r}-\boldsymbol{r}_B) \end{aligned} \tag{3.8}$$

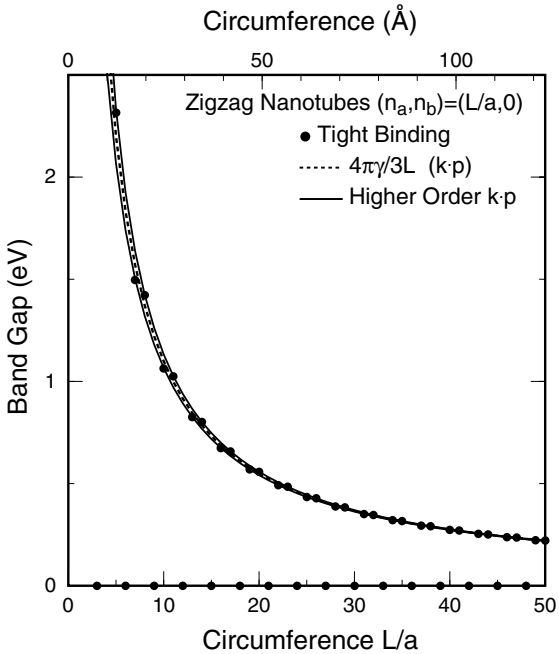

Figure 8. The bandgap of a zigzag nanotube as a function of the circumference L/a. The dots represent tight-binding results and the dotted line the result of the lowest-order $\boldsymbol{k}\cdot\boldsymbol{p}$ scheme. When higher-order $\boldsymbol{k}\cdot\boldsymbol{p}$ terms are included, a small deviation present in figure 5 is removed almost completely.

with

$$\begin{aligned} u_A &= \frac{\sqrt{3}a^2}{2}\sum_{\boldsymbol{R}_A} u_A(\boldsymbol{R}_A) \\ u_B &= \frac{\sqrt{3}a^2}{2}\sum_{\boldsymbol{R}_B} u_B(\boldsymbol{R}_B) \\ u'_A &= \frac{\sqrt{3}a^2}{2}\sum_{\boldsymbol{R}_A} \mathrm{e}^{\mathrm{i}(\boldsymbol{K}'-\boldsymbol{K})\cdot\boldsymbol{R}_A}u_A(\boldsymbol{R}_A) \\ u'_B &= \frac{\sqrt{3}a^2}{2}\sum_{\boldsymbol{R}_B} \mathrm{e}^{\mathrm{i}(\boldsymbol{K}'-\boldsymbol{K})\cdot\boldsymbol{R}_B}u_B(\boldsymbol{R}_B) \end{aligned} \tag{3.9}$$

where $\boldsymbol{r}_A$ and $\boldsymbol{r}_B$ are the centre-of-mass position of the effective impurity potential and $\sqrt{3}a^2/2$ is the area of a unit cell. The integrated intensities u_A, etc given by equation (3.9) have been obtained by the $\boldsymbol{r}$ integral of $u_A(\boldsymbol{r})$, etc given by equation (3.6) and using equation (3.7).

In the vicinity of $\varepsilon = 0$, we have two right-going channels $K+$ and K′+, and two left-going channels $K-$ and K′−. The matrix elements are calculated as [50]

$$\begin{aligned} V_{K\pm K+} &= V_{K'\pm K'+} = \tfrac{1}{2}(\pm u_A + u_B) \\ V_{K\pm K'+} &= V^*_{K'\pm K+} = \tfrac{1}{2}(\mp u'_A\,\mathrm{e}^{\mathrm{i}\eta} - \omega^{-1}\mathrm{e}^{-\mathrm{i}\eta}u'_B). \end{aligned} \tag{3.10}$$

When the impurity potential has a range larger than the lattice constant, we have $u_A = u_B$ and both u'_A and u'_B become much smaller and can be neglected because of the phase factor $\mathrm{e}^{\mathrm{i}(\boldsymbol{K}'-\boldsymbol{K})\cdot\boldsymbol{R}_A}$ and $\mathrm{e}^{\mathrm{i}(\boldsymbol{K}'-\boldsymbol{K})\cdot\boldsymbol{R}_B}$. This means that intervalley scattering between K and K′ points can be neglected for such impurities as usually assumed in the conventional $\boldsymbol{k}\cdot\boldsymbol{p}$ approximation. Further, the above shows that the backward

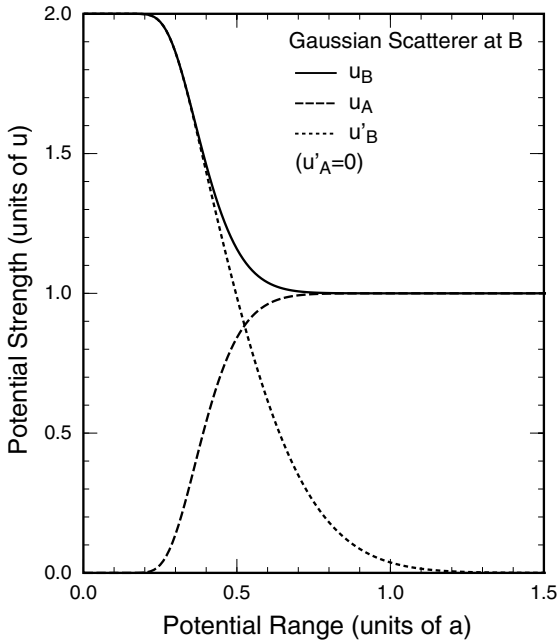

Figure 9. Calculated effective strength of the potential for a model Gaussian impurity at a B site. After [50].

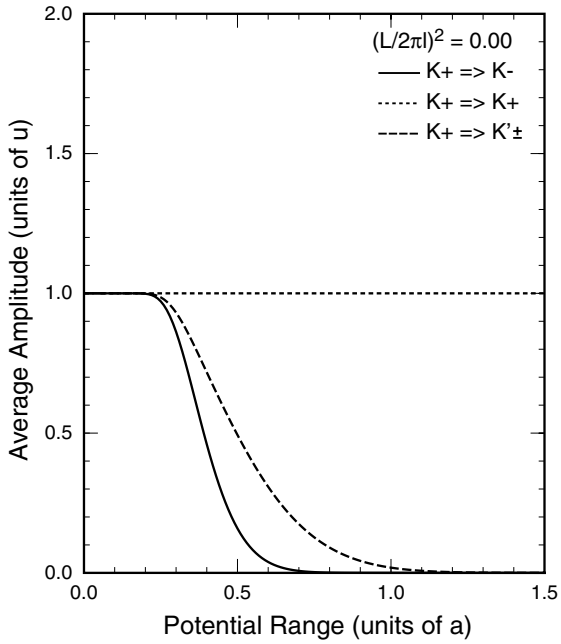

Figure 10. Calculated effective scattering matrix elements versus the potential range at $\varepsilon = 0$ in the absence of a magnetic field. After [50].

scattering probability within each valley vanishes in the lowest Born approximation.

Figure 9 gives an example of calculated effective potential u_A, u_B and u'_B as a function of d/a for a Gaussian potential located at a B site and having the integrated intensity u. Because of the symmetry corresponding to a 120° rotation around a lattice point, we have $u'_A = 0$ independent of d/a. When the range is sufficiently small, u_B and u'_B stay close to $2u$ because the potential is localized only at the impurity B site. With the increase of d the potential becomes nonzero at neighbouring A sites and u_A starts to increase and at the same time both u_B and u'_B decrease. The diagonal elements u_A and u_B rapidly approach u and the off-diagonal element u'_B vanishes.

Figure 10 shows calculated averaged scattering amplitude, given by $AL\sqrt{\langle|V_{K\pm K+}|^2\rangle}$ and $AL\sqrt{\langle|V_{K'\pm K+}|^2\rangle}$ where $\langle|V_{K\pm K+}|^2\rangle$ and $\langle|V_{K'\pm K+}|^2\rangle$ are the squared matrix elements averaged over impurity position, as a function of d in the absence of a magnetic field. The backward scattering probability decreases rapidly with d and becomes exponentially small for $d/a \gg 1$. The same is true of the intervalley scattering although the dependence is slightly weaker because of the slower decrease of u'_B shown in figure 9.

This absence of the backward scattering for long-range scatterers disappears in the presence of magnetic fields as shown in figure 11. In high magnetic fields, the intervalley scattering is reduced considerably because of the reduction in the overlap of the wavefunction as shown in equation (2.8), but the intravalley backward scattering remains nonzero.

The Boltzmann conductivity can be calculated in a straightforward manner by solving a transport equation in a way developed for quantum wires [51, 52]. In the limit of

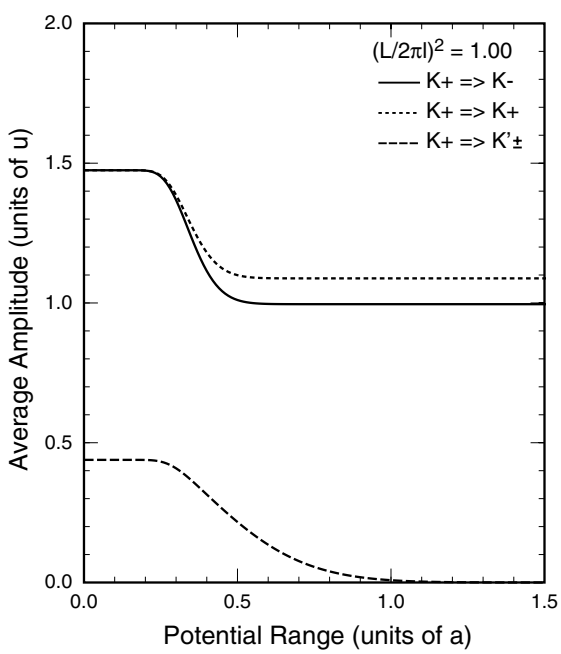

Figure 11. Calculated effective scattering matrix elements versus the potential range at $\varepsilon = 0$ in the magnetic field corresponding to $(L/2\pi l)^2 = 1$. After [50].

short-range scatterers $d/a \ll 1$, in particular, we have

$$\sigma = \frac{2\sigma_0}{I_0(4\alpha)} \tag{3.11}$$

with

$$\sigma_0 = \frac{4e^2}{\pi\hbar}\Lambda \qquad \Lambda = \frac{\tau\gamma}{\hbar} \qquad \frac{\hbar}{\tau} = \frac{4n_i\langle u^2\rangle}{\gamma L} \tag{3.12}$$

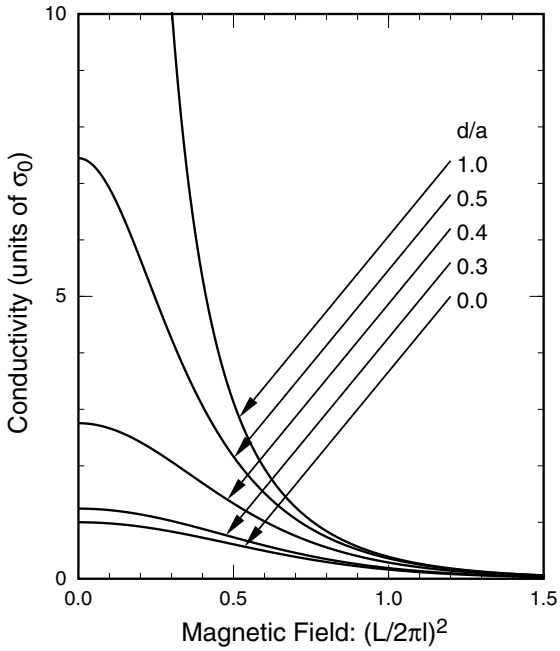

Figure 12. Calculated conductivity at $\varepsilon = 0$ as a function of the effective magnetic field $(L/2\pi l)^2$ for various values of d/a. In the absence of a magnetic field, i.e., at $(L/2\pi l)^2 = 0$, the conductivity becomes extremely large for $d/a > 1$. After [50].

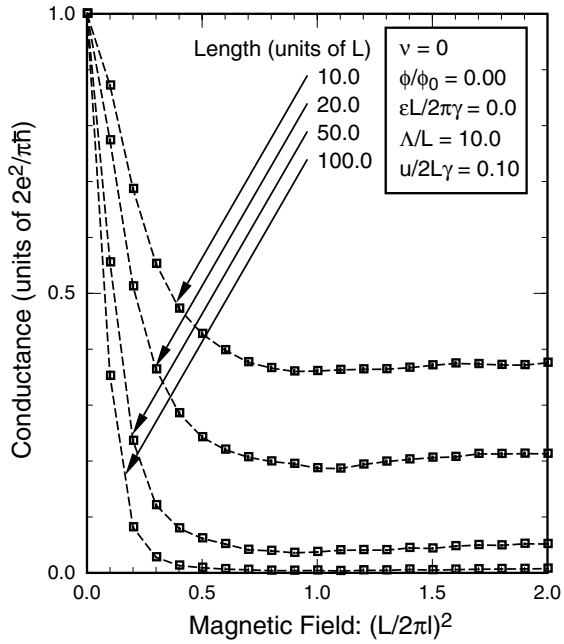

Figure 13. Calculated conductance of finite-length nanotubes at $\varepsilon = 0$ as a function of the effective strength of a magnetic field $(L/2\pi l)^2$ in the case where the effective mean free path Λ is much larger than the circumference L. The conductance is always given by the value in the absence of impurities at $H = 0$. After [50].

where n_i is the impurity concentration per unit area and $\langle u^2 \rangle = \langle u_A^2 \rangle = \langle u_B^2 \rangle = \langle |u'_A|^2 \rangle = \langle |u'_B|^2 \rangle$. Figure 12 gives examples of the calculated Boltzmann conductivity as a function of the effective magnetic field $(L/2\pi l)^2$. The positive magnetoresistance present even for $d/a \ll 1$ becomes stronger with the increase of d/a. The conductivity in the absence of a magnetic field is extremely large when $d/a > 1$ because of the vanishing backward scattering probability.

It is straightforward to calculate a scattering matrix for an impurity given by equation (3.8) and a conductance of a finite-length nanotube containing many impurities, combining S matrices [48, 50]. Figure 13 shows some examples of calculated conductance at $\varepsilon = 0$ in the case where the impurity potential has a range larger than the lattice constant, i.e., $u_A = u_B = u$. A typical mean free path Λ defined in equation (3.12) for the present u is $\Lambda/L = 10$ (the definition of Λ is actually quite ambiguous because of the singular dependence on the magnetic field). The conductance in the absence of a magnetic field is always quantized into $2e^2/\pi\hbar$ because of the complete absence of backward scattering. With the increase of the magnetic field the conductance is reduced drastically and the amount of the reduction becomes larger with the increase of the length.

In strong magnetic fields the conductance becomes nearly independent of the field strength and is roughly proportional to the inverse of the length. This behaviour can be understood by the fact that the conductivity of the 2D graphite is given by $2e^2/\pi\hbar$ independent of a magnetic field at $\varepsilon = 0$ [53] and the conductance of the CN is approximately given by the conductivity of the 2D graphite multiplied by the circumference and divided by the length.

It has been proved that the Born series for back-scattering vanishes identically [50]. This can be ascribed to a spinor-type property of the wave function under a rotation in the wave vector space [54]. In fact, an electron in the nanotube can be regarded as a neutrino, which has a helicity, i.e., its spin is always quantized into the direction of its wave vector, and therefore each scattering corresponds to a spin rotation. When the potential range is sufficiently large, i.e., $u_A(\boldsymbol{r}) = u_B(\boldsymbol{r})$ and $u'_A(\boldsymbol{r}) = u'_B(\boldsymbol{r}) = 0$, a matrix element for scattering is separable into a product of that of the impurity potential and a spin rotation.

A back-scattering corresponds to a spin rotation by $+(2n+1)\pi$ with n being an appropriate integer and its time reversal process corresponds to a spin rotation by $-(2n+1)\pi$. The spinor wave function after a rotation by $-(2n+1)\pi$ has a signature opposite to that after a rotation by $+(2n+1)\pi$ because of a well known property of a spin-rotation operator. On the other hand, the matrix element of the time reversal process has an identical spatial part. As a result, the sum of the matrix elements of a back-scattering process and its time reversal process cancels out completely, leading to the absence of backward scattering.

The spin in the present Schrödinger equation is not a real spin but a pseudo-spin describing the relative amplitude of the wave function at A and B sublattices. Therefore, the phase due to the rotation should be regarded as Berry's phase [55, 56].

A weak backward scattering becomes possible if effects of higher-order $\boldsymbol{k} \cdot \boldsymbol{p}$ terms giving a trigonal warping of the bands are included [54]. The scattering probability for potential $V(\boldsymbol{r})$ from a state $k_y = +k$ to $-k$ is calculated as

$$(ka)^2 \cos^2 3\eta |V(-2k)|^2 \tag{3.13}$$

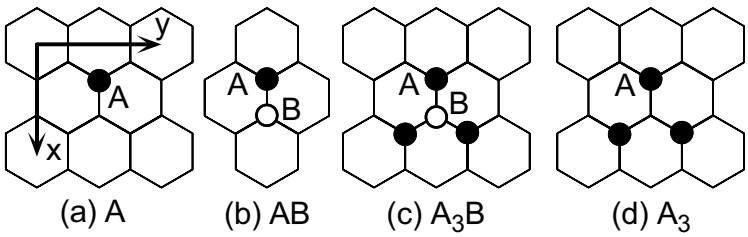

Figure 14. Schematic illustration of vacancies in an armchair nanotube. The closed and open circles denote A and B lattice points, respectively. (a) A, (b) AB, (c) A_3B and (d) A_3.

in the lowest-order Born approximation, with

$$V(-2k) = \iint \mathrm{d}x\,\mathrm{d}y\,V(\boldsymbol{r})\exp(2iky). \tag{3.14}$$

The backward scattering increases in proportion to ε^2 except in the case of armchair nanotubes for which $\eta = \pi/6$. These results were confirmed by a numerical calculation in a tight-binding model [57].

The magnetoresistance of bundles of multi-wall nanotubes was measured and a negative magnetoresistance was observed in sufficiently low magnetic fields and at low temperatures [24]. With the increase of the magnetic field the resistance starts to exhibit a prominent positive magnetoresistance. This positive magnetoresistance is in qualitative agreement with the theoretical prediction of the reappearance of backscattering in magnetic fields.

Measurements of the resistance of a single multi-wall nanotube were reported [27–32] and irregular oscillation analogous to universal conductance fluctuations was observed [27]. A resistance oscillation more regular like that of an Aharonov–Bohm type was observed in a magnetic field parallel to the CN axis [58]. Recently observed resistance oscillation in a parallel field was shown to be consistent with the Aharonov–Bohm oscillation of the bandgap due to a magnetic flux passing through the CN cross section [59].

Because of the presence of large contact resistance between a nanotube and metallic electrode, the measurement of the conductance of a nanotube itself is quite difficult and has not been so successful. However, from measurements of single-electron tunnelling due to a Coulomb blockade and charging effect, important information can be obtained on the effective mean free path and the amount of backward scattering in nanotubes [33–37]. Discrete quantized energy levels were measured for a nanotube with ~ 3 μm length, for example, showing that the electron wave is coherent and extended over the whole length.

It was shown further that the Coulomb oscillation in semiconducting nanotubes is quite irregular and can be explained only if nanotubes are divided into many separate spatial regions in contrast to that in metallic nanotubes [60]. This behaviour is consistent with the presence of a considerable amount of backward scattering leading to a strong localization of the electron wave function in semiconducting tubes. In metallic nanotubes, the wave function is extended throughout the whole region of a nanotube because of the absence of backward scattering.

A conductance quantization was observed in multi-wall nanotubes [61]. This quantization is likely to be related to the absence of backward scattering shown here, but much more work is necessary including effects of magnetic fields and problems related to contacts with a metallic electrode before complete understanding of the experimental result. At room temperature, where the experiment was performed, phonon scattering is likely to play an important role [25, 62–64].

4. Lattice vacancies

Some experiments suggest the existence of defective nanotubes of carpet-roll or papier mâché forms [65, 66]. These systems have many disconnections of the π electron network governing transport of CNs and therefore are expected to exhibit properties different from those in perfect CNs. In a graphite sheet with a finite width, for examples localized edge states are formed at $\varepsilon = 0$, when the boundary is in a certain specific direction [67–69].

Effects of scattering by a vacancy in armchair nanotubes have been studied within a tight-binding model [70–72]. Figure 14 shows three typical vacancies: (a) vacancy I, (b) vacancy IV and (c) vacancy II. In the vacancy I a single carbon site (site A) is removed, in the vacancy IV one A site and three B sites are removed, and in the vacancy II a pair of A and B sites are removed. The vacancy (d) is equivalent to (c). It has been shown that the conductance at $\varepsilon = 0$ in the absence of a magnetic field is quantized into zero, one or two times the conductance quantum $e^2/\pi\hbar$ for vacancy IV, I and II, respectively [71, 72].

Figure 15 shows the calculated conductance as a function of the Fermi energy between $\varepsilon = 0$ and $\varepsilon = \varepsilon(1)$, where $\varepsilon(1)$ is the energy of the bottom of the first excited band ($\varepsilon(1) = 2\pi\gamma/L$ in the $\boldsymbol{k}\cdot\boldsymbol{p}$ scheme). For the vacancy I, the conductance at $\varepsilon = 0$ is the half of that in a defect free system. Both intra- and inter-valley components have an equal amplitude for both transmission and reflection processes, i.e., $|t_{\mu\nu}|^2 = |r_{\mu\nu}|^2 = 1/4$. The conductance increases as a function of ε for $0 < \varepsilon < \varepsilon(1)$ and reaches $2e^2/\pi\hbar$ at $\varepsilon = \varepsilon(1)$, where a perfect transmission occurs, i.e., $t_{KK} = t_{K'K'} = 1$. Except at $\varepsilon = 0$ and $\varepsilon = \varepsilon(1)$, the conductance increases with the increase of the circumference.

In CNs with the vacancy IV, the conductance at $\varepsilon = 0$ vanishes as shown in figure 15(b) and a perfect reflection occurs within the same valley, i.e., $|r_{KK}| = |r_{K'K'}| = 1$. The conductance increases with increasing ε and reaches $2e^2/\pi\hbar$ at $\varepsilon = \varepsilon(1)$. Except at $\varepsilon = 0$ and $\varepsilon = \varepsilon(1)$, the conductance increases with increasing L.

In CNs with the vacancy II, the conductance around $\varepsilon = 0$ is slightly smaller than $2e^2/\pi\hbar$ and gradually increases

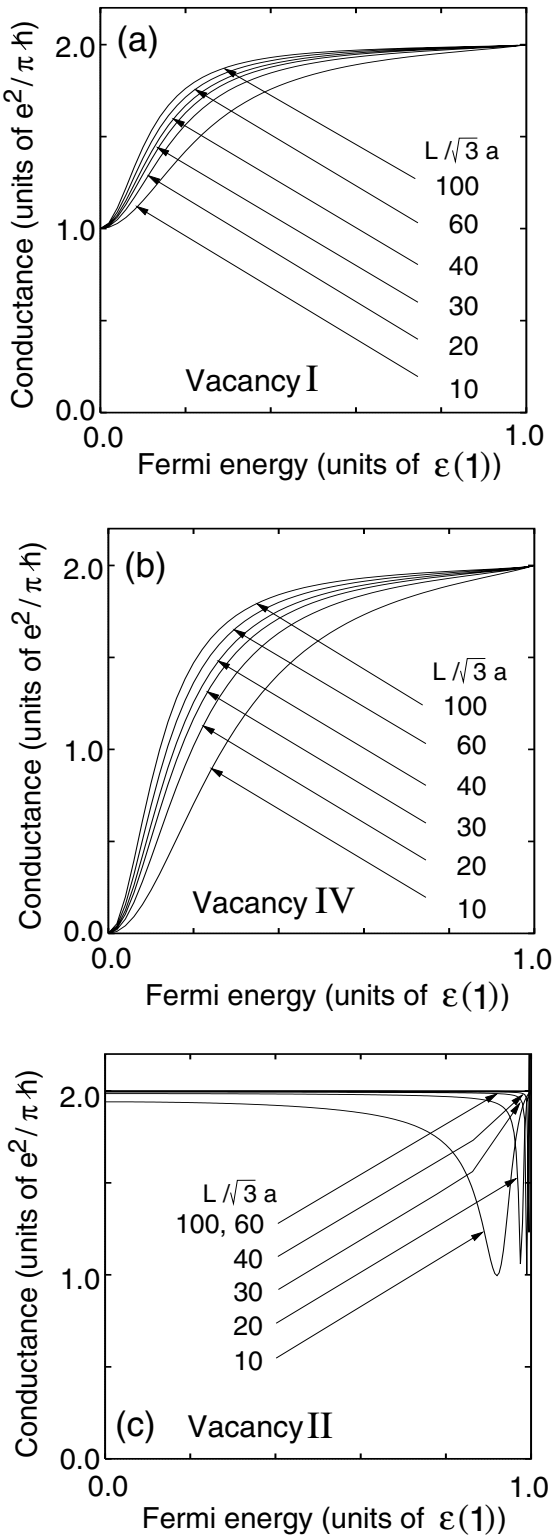

Figure 15. Calculated conductance in units of $e^2/\pi\hbar$ as a function of the Fermi energy for CNs with vacancy I (a), IV (b) and II (c), where the energy is scaled by $\varepsilon(1)$, which corresponds to the bottom of the second conduction bands. After [71].

and approaches $2e^2/\pi\hbar$ with the increase of the radius as shown in figure 15(c). The deviation from the perfect conductance $2e^2/\pi\hbar$ decreases with the increase of L in proportion to $(a/L)^2$. The conductance exhibits a dip at the energy slightly below $\varepsilon = \varepsilon(1)$, but reaches $2e^2/\pi\hbar$ at $\varepsilon = \varepsilon(1)$. The back-scattering within each valley r_{KK} and $r_{K'K'}$ and the transmission between different valleys $t_{KK'}$ and $t_{K'K}$ are absent because of a mirror symmetry about a plane containing the axis.

Numerical calculations were performed for about 1.5×10^5 vacancies and demonstrated that such quantization is quite general [73]. Let N_A and N_B be the number of removed atoms at A and B sublattice points, respectively, and $\Delta N_{AB} = N_A - N_B$. Then, the numerical results show that for vacancies much smaller than the circumference, the conductance vanishes for $|\Delta N_{AB}| \geqslant 2$ and quantized into one and two times $e^2/\pi\hbar$ for $|\Delta N_{AB}| = 1$ and 0, respectively.

Effects of the vacancy I in armchair nanotubes were studied in a similar tight-binding model [70], in which the conductance at $\varepsilon = 0$ was claimed to approach $2e^2/\pi\hbar$ with increasing L. It is likely, however, that the results do not exactly correspond to $\varepsilon = 0$ but to a small but nonzero value. In fact, if the conductance obtained above is plotted against L for $\varepsilon/\gamma_0 = 0.02$, the resulting curve is almost same as that given in figure 3 of [70].

Effects of impurities with a strong and short-range potential can be studied also in a $\boldsymbol{k}\cdot\boldsymbol{p}$ scheme [74]. For an impurity localized at a carbon A site $\boldsymbol{r}_j$ and having the integrated intensity u, we have [50]

$$V(\boldsymbol{r}) = V_j\delta(\boldsymbol{r} - \boldsymbol{r}_j) \tag{4.1}$$

with

$$V_j = u\begin{pmatrix} 1 & 0 & \mathrm{e}^{\mathrm{i}\phi_j^A} & 0 \\ 0 & 0 & 0 & 0 \\ \mathrm{e}^{-\mathrm{i}\phi_j^A} & 0 & 1 & 0 \\ 0 & 0 & 0 & 0 \end{pmatrix} \tag{4.2}$$

and

$$\phi_j^A = (\boldsymbol{K}' - \boldsymbol{K})\cdot\boldsymbol{r}_j + \eta. \tag{4.3}$$

For an impurity at a carbon B site we have

$$V_j = u\begin{pmatrix} 0 & 0 & 0 & 0 \\ 0 & 1 & 0 & \mathrm{e}^{\mathrm{i}\phi_j^B} \\ 0 & 0 & 0 & 0 \\ 0 & \mathrm{e}^{-\mathrm{i}\phi_j^B} & 0 & 1 \end{pmatrix} \tag{4.4}$$

with

$$\phi_j^B = (\boldsymbol{K}' - \boldsymbol{K})\cdot\boldsymbol{r}_j - \eta + \frac{\pi}{3}. \tag{4.5}$$

The scattering matrix can be written formally as

$$S = S^{(0)} + S^{(1)} \tag{4.6}$$

with

$$S^{(0)}_{\alpha\beta} = \delta_{\alpha\beta} \tag{4.7}$$

and

$$S^{(1)}_{\alpha\beta} = -\mathrm{i}\frac{A}{\hbar\sqrt{|v_\alpha v_\beta|}}T_{\alpha\beta} \tag{4.8}$$

where v_α and v_β are the velocity of channels α and β. The T matrix satisfies

$$T = V + V\frac{1}{\varepsilon - \mathcal{H}_0 + \mathrm{i}0}V + V\frac{1}{\varepsilon - \mathcal{H}_0 + \mathrm{i}0}V\frac{1}{\varepsilon - \mathcal{H}_0 + \mathrm{i}0}V + \cdots \tag{4.9}$$

which is solved as

$$(\alpha|T|\beta) = \sum_{ij} \boldsymbol{f}_\alpha^+ T_{ij} \boldsymbol{f}_\beta \exp(-\mathrm{i}\kappa_\alpha x_i - \mathrm{i}k_\alpha y_i) \times \exp(\mathrm{i}\kappa_\beta x_j + \mathrm{i}k_\beta y_j) \tag{4.10}$$

where κ_α and κ_β are the wave vectors in the circumference direction corresponding to channel α and β, k_α and k_β are the wave vectors in the axis direction, $\boldsymbol{f}_\alpha$ and $\boldsymbol{f}_\beta$ are corresponding eigenvectors defined by

$$\boldsymbol{F}_\alpha(\boldsymbol{r}) = \frac{1}{\sqrt{LA}} \boldsymbol{f}_\alpha \exp(\mathrm{i}\kappa_\alpha x + \mathrm{i}k_\alpha y) \qquad \text{etc} \tag{4.11}$$

and

$$T_{ij} = \left[\left(1 - \frac{1}{AL} V G(\varepsilon + \mathrm{i}0) \right)^{-1} \frac{1}{AL} V \right]_{ij} \tag{4.12}$$

with $V_{jj'} = V_j \delta_{jj'}$. The Green function $G_{ij} = G(\boldsymbol{r}_i - \boldsymbol{r}_j)$ is written as

$$G(\boldsymbol{r}) = \frac{-\mathrm{i}A}{2\gamma} \begin{pmatrix} g_0 & g_1 & 0 & 0 \\ \bar{g}_1 & g_0 & 0 & 0 \\ 0 & 0 & g_0 & \bar{g}_1 \\ 0 & 0 & g_1 & g_0 \end{pmatrix} \tag{4.13}$$

where

$$g_0(x, y) = \frac{\mathrm{i}\gamma}{\pi} \int \mathrm{d}k \times \sum_n f_c[\kappa(n), k] \frac{\varepsilon\, \mathrm{e}^{\mathrm{i}\kappa(n)x + \mathrm{i}ky}}{(\varepsilon + \mathrm{i}0)^2 - \gamma^2[\kappa(n)^2 + k^2]}$$

$$g_1(x, y) = \frac{\mathrm{i}\gamma}{\pi} \int \mathrm{d}k \times \sum_n f_c[\kappa(n), k] \frac{\gamma[\kappa(n) - \mathrm{i}k]\, \mathrm{e}^{\mathrm{i}\kappa(n)x + \mathrm{i}ky}}{(\varepsilon + \mathrm{i}0)^2 - \gamma^2[\kappa(n)^2 + k^2]} \tag{4.14}$$

and $\bar{g}_1(x, y) = g_1(x, -y)$. We have introduced a cutoff function $f_c[\kappa(n), k]$ defined by

$$f_c[\kappa(n), k] = \frac{k_c^2}{k^2 + \kappa(n)^2 + k_c^2} \tag{4.15}$$

in order to extract the contribution from states in the vicinity of the Fermi level. The cutoff wave vector k_c is determined by the condition that the cutoff wavelength $2\pi/k_c$ should be comparable to the lattice constant a, i.e., $2\pi/k_c \approx a$.

At $\varepsilon = 0$, in particular, we have

$$g_0(x, y) = 1 \tag{4.16}$$

and

$$g_1(x, y) = \frac{\cos[\pi(x + \mathrm{i}y)/L]}{\sin[\pi(x + \mathrm{i}y)/L]}. \tag{4.17}$$

The off-diagonal Green function g_1 is singular in the vicinity of $\boldsymbol{r} = \boldsymbol{0}$. Therefore, for impurities localized within a distance of a few times the lattice constant, the off-diagonal Green function becomes extremely large. This singular behaviour is the origin of the peculiar dependence of the conductance on the difference in the number of vacancies at A and B sublattices.

For a few impurities, the T matrix can be obtained analytically and becomes equivalent to that of lattice vacancies in the limit of strong scatterers, i.e., $|u|/2\gamma L \gg 1$. In particular, the tight-binding results shown in Figure 15 are reproduced quite well. In the limit of $a/L \to 0$ and a strong scatterer the behaviour of the conductance at $\varepsilon = 0$ can be studied analytically for arbitrary values of N_A and N_B. The results explain the numerical tight-binding result that $G = 0$ for $|\Delta N_{AB}| \geqslant 2$, $G = e^2/\pi\hbar$ for $|\Delta N_{AB}| = 1$ and $G = 2e^2/\pi\hbar$ for $\Delta N_{AB} = 0$.

The origin of this interesting dependence on N_A and N_B is a reduction of the scattering potential by multiple scattering on a pair of A and B scatterers. In fact, multiple scattering between an A impurity at $\boldsymbol{r}_i$ and a B impurity at $\boldsymbol{r}_j$ reduces their effective potential by the factor $|g_1(\boldsymbol{r}_i - \boldsymbol{r}_j)|^{-2} \propto (a/L)^2$. By eliminating AB pairs successively, some A or B impurities remain. The conductance is determined essentially by the number of these unpaired impurities.

Such a direct elimination procedure is not rigorous because there are many different ways to eliminate AB pairs and multiple scattering between unpaired and eliminated impurities cannot be neglected completely because of large off-diagonal Green functions. However, a correct mathematical procedure can be formulated in which a proper combination of A and B impurities leads to a vanishing scattering potential and the residual potential is determined by another combination of remaining A or B impurities.

Effects of a magnetic field were studied for three types of vacancies shown in figure 14. [71]. The results show a universal dependence on the field component in the direction of the vacancy position. There are various other theoretical calculations in tight-binding models of electronic states and transport of tubes containing lattice defects [75] or disorder [76–80].

5. Junctions of nanotubes

A junction which connects CNs with different diameters through a region sandwiched by a pentagon–heptagon pair has been observed in the transmission electron microscope [2]. Figure 16(a) shows such an example and figure 16(b) bend junctions [81]. Some theoretical calculations on CN junctions within a tight-binding model were reported for junctions between metallic and semiconducting nanotubes and those between semiconducting nanotubes [82, 83]. In particular tight-binding calculations for junctions consisting of two metallic tubes with different chirality or diameter demonstrated the conductance exhibits a universal power-law dependence on the ratio of the circumference of two nanotubes [84–86]. The $\boldsymbol{k} \cdot \boldsymbol{p}$ scheme is ideal to clarify electronic states and their topological characteristics in such junction systems.

Figure 17 shows the development of a junction system into a 2D graphite sheet [83]. We separate the development into three regions, the thick tube, the junction region and the thin tube. We have a pair of a pentagon ($\boldsymbol{R}_5$) and heptagon ($\boldsymbol{R}_7$) ring, and $\boldsymbol{L}_5$ and $\boldsymbol{L}_7$ are the chiral vector of the thick and thin nanotube, respectively. Therefore, $\boldsymbol{R}_5 - \boldsymbol{L}_5$ and $\boldsymbol{R}_7 - \boldsymbol{L}_7$ are rolled on to $\boldsymbol{R}_5$ and $\boldsymbol{R}_7$, respectively. An equilateral triangle with a base connecting $\boldsymbol{R}_5$ and $\boldsymbol{R}_5 - \boldsymbol{L}_7$ and another with a base connecting $\boldsymbol{R}_7$ and $\boldsymbol{R}_7 - \boldsymbol{L}_7$ have a common vertex point at $\boldsymbol{R}$. We choose both the origin of the

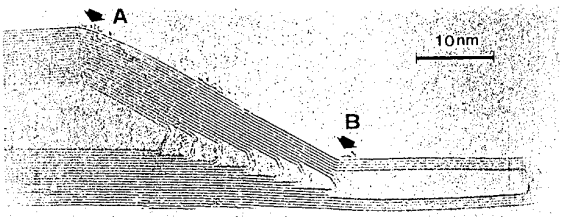

(a)

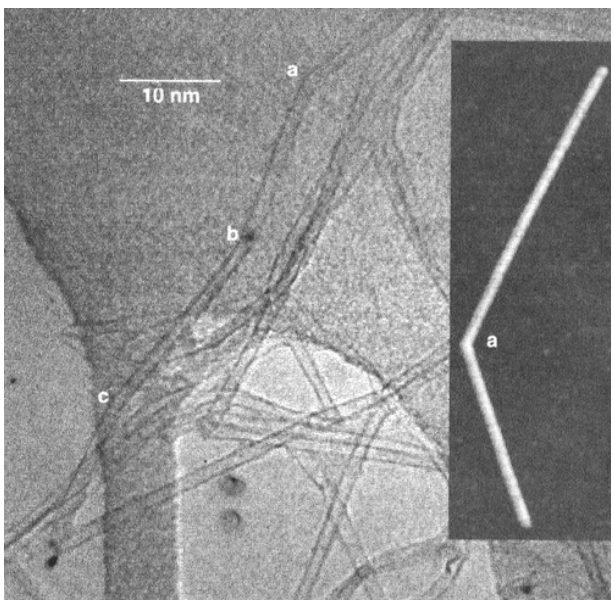

(b)

Figure 16. Transmission micrograph image of (a) a tip of a carbon nanotube [2] and (b) bend junctions [81].

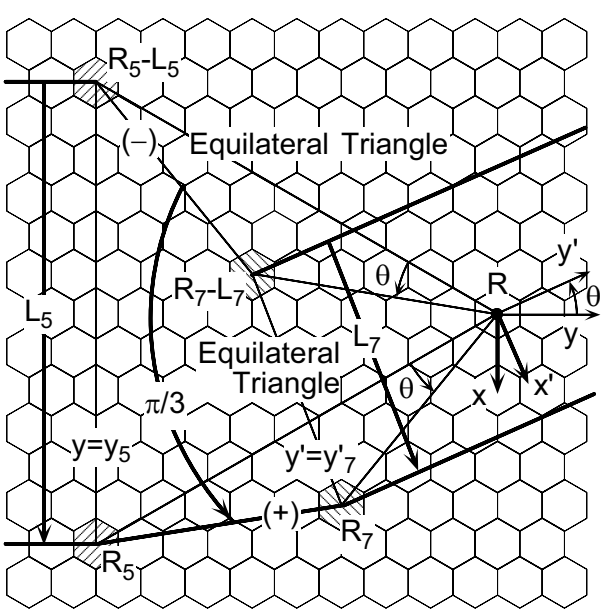

Figure 17. The structure of a junction consisting of two nanotubes having axes not parallel to each other (θ is their angle).

(x, y) coordinate fixed onto the thick nanotube and that of the (x', y') coordinate fixed on the thin nanotube at $\boldsymbol{R}$. The angle between $\boldsymbol{L}_5$ and $\boldsymbol{L}_7$ is denoted as θ.

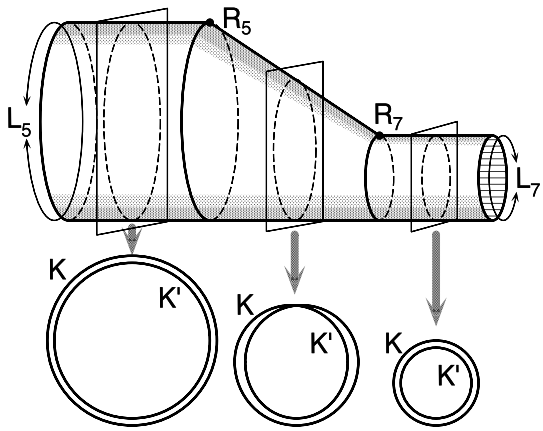

Figure 18. Schematic illustration of the topological structure of a junction. In the tube regions, two cylinders corresponding to spaces for the K and K′ points are independent of each other. In the junction region, they are interconnected to each other.

Boundary conditions can be derived by considering such a structure of junction [87]. In the junction region, any point on the development moves onto the corresponding point after making a rotation by $\pi/3$ around $\boldsymbol{R}$ as shown in figure 17. Then, we have

$$\boldsymbol{F}[R_{\pi/3}\boldsymbol{r}] = T_{\pi/3}\boldsymbol{F}(\boldsymbol{r})$$

$$T_{\pi/3} = \begin{pmatrix} 0 & 0 & 0 & \mathrm{e}^{\mathrm{i}\psi(\boldsymbol{R})} \\ 0 & 0 & -\omega^{-1}\,\mathrm{e}^{\mathrm{i}\psi(\boldsymbol{R})} & 0 \\ 0 & -\mathrm{e}^{-\mathrm{i}\psi(\boldsymbol{R})} & 0 & 0 \\ \omega\,\mathrm{e}^{-\mathrm{i}\psi(\boldsymbol{R})} & 0 & 0 & 0 \end{pmatrix} \tag{5.1}$$

with

$$\mathrm{e}^{\mathrm{i}\psi(\boldsymbol{R})} = \exp[\mathrm{i}(\boldsymbol{K}' - \boldsymbol{K})\cdot\boldsymbol{R}] \tag{5.2}$$

where $\omega = \exp(2\pi\,\mathrm{i}/3)$ and $R_{\pi/3}$ describes a $\pi/3$ rotation around $\boldsymbol{R}$. Because of the boundary conditions, states near the K and K′ point mix together in the junction region. Figure 18 shows the topological structure of the junction system.

Under these boundary conditions, the Schrödinger equation has solutions which are represented in the polar coordinates (r, ϕ) with Bessel $Z_\mu = J_\mu$ and Neumann functions $Z_\mu = N_\mu$ by

$$\boldsymbol{F}_\mu^Z = \frac{1}{\sqrt{L_5}} \begin{pmatrix} Z_{3\mu+1}(kr)\,\mathrm{e}^{\mathrm{i}(3\mu+1)\phi} \\ \mathrm{i}\,\mathrm{sgn}(\varepsilon) Z_{3\mu+2}(kr)\,\mathrm{e}^{\mathrm{i}(3\mu+1)\phi} \\ (-)^\mu \mathrm{i}\,\mathrm{sgn}(\varepsilon) Z_{3\mu+2}(kr)\,\mathrm{e}^{\mathrm{i}(3\mu+1)\phi} \\ (-)^\mu Z_{3\mu+1}(kr)\,\mathrm{e}^{\mathrm{i}(3\mu+1)\phi} \end{pmatrix} \tag{5.3}$$

where μ is an integer, $\mathrm{sgn}(t) = +1$ for $t > 0$ and $\mathrm{sgn}(t) = -1$ for $t < 0$, and $k = |\varepsilon|/\gamma$. In particular when the energy is equal to the Fermi energy ($\varepsilon = 0$), these solutions become [87]

$$\boldsymbol{F}_m^A = \frac{1}{\sqrt{L_5}} \begin{pmatrix} 1 \\ 0 \\ 0 \\ (-1)^m \end{pmatrix} \left(\frac{+\mathrm{i}z}{L_5}\right)^{3m+1}$$

$$\boldsymbol{F}_m^B = \frac{1}{\sqrt{L_5}} \begin{pmatrix} 0 \\ 1 \\ (-1)^{m+1} \\ 0 \end{pmatrix} \left(\frac{-\mathrm{i}\bar{z}}{L_5}\right)^{3m+1} \tag{5.4}$$

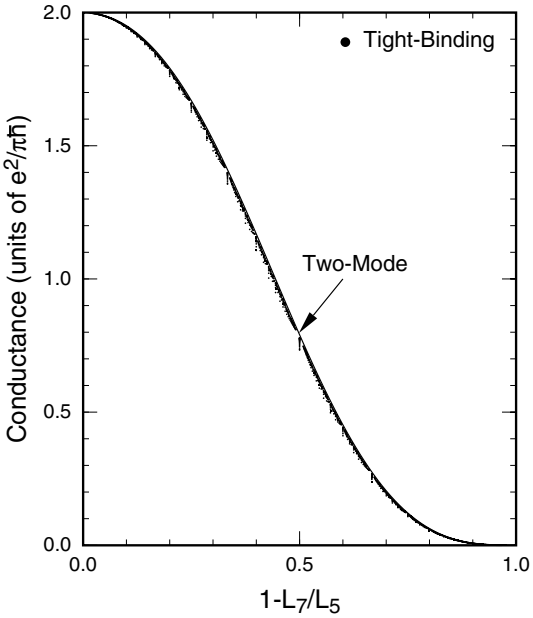

Figure 19. The conductance obtained in the two-mode approximation and tight-binding results of armchair and zigzag nanotubes versus the effective length of the junction region $(L_5 - L_7)/L_5$. After [87].

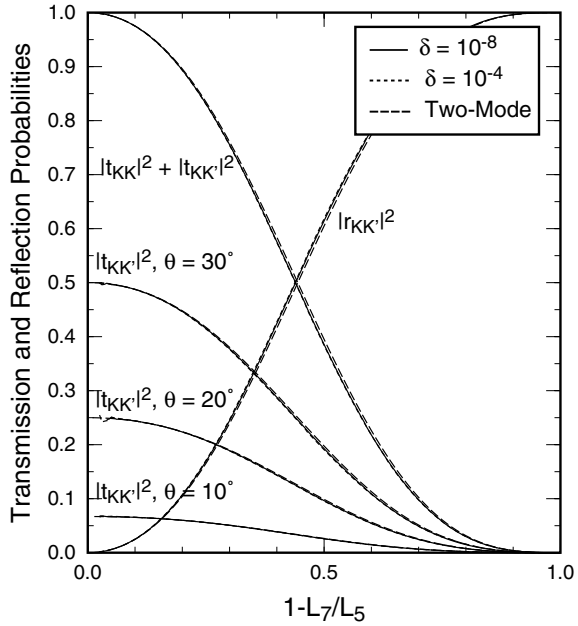

Figure 20. Calculated transmission and reflection probabilities versus the effective length of the junction region $(L_5 - L_7)/L_5$. Contributions of intervalley scattering to the transmission are plotted for $\theta = 10^\circ$, 20° and 30°. The results are almost independent of the value of δ. After [89].

where m is an integer, $z = x + \mathrm{i}y$ and $\bar{z} = x - \mathrm{i}y$.

We put the right-going wave from the left side of the junction (through the thicker tube). To obtain the overall wave function of the system, we should connect these three types of solution at the boundary $y = y_5$ (the line connecting $\boldsymbol{R}_5$ and $\boldsymbol{R}_5 - \boldsymbol{L}_5$ in figure 17) and at $y' = y'_7$ (the line connecting $\boldsymbol{R}_7$ and $\boldsymbol{R}_7 - \boldsymbol{L}_7$).

An approximate expression for the transmission T and reflection probabilities R can be obtained by neglecting evanescent modes decaying exponentially into the thick and thin nanotubes. The solution gives

$$T = \frac{4L_5^3 L_7^3}{(L_5^3 + L_7^3)^2} \qquad R = \frac{(L_5^3 - L_7^3)^2}{(L_5^3 + L_7^3)^2}. \tag{5.5}$$

We have $T \sim 4(L_7/L_5)^3$ in the long junction ($L_7/L_5 \ll 1$). When they are separated into different components,

$$T_{KK} = T\cos^2(\tfrac{3}{2}\theta) \qquad T_{KK'} = T\sin^2(\tfrac{3}{2}\theta) \tag{5.6}$$

and

$$R_{KK} = 0 \qquad R_{KK'} = R \tag{5.7}$$

where the subscript KK means intravalley scattering within the K or K′ points and KK′ stands for intervalley scattering between K and K′ points. As for the reflection, no intravalley scattering is allowed. The dependence on the tilt angle θ originates from two effects. One is $\theta/2$ arising from the spinor-like character of the wave function in the rotation θ. Another θ comes from the junction wave function with $m = 0$ which decays most slowly along the y axis. Figure 19 shows a comparison of the two-mode solution with tight-binding results [84, 85, 88] for $\theta = 0$.

In actual calculations, we have to limit the total number of eigenmodes in both nanotube and junction regions. In the junction region the wave function for $m \geqslant 0$ decays and that for $m < 0$ becomes larger in the positive y direction. We shall choose cutoff M of the number of eigenmodes in the junction region, i.e., $-M - 1 \leqslant m \leqslant M$, for a given value of L_7/L_5 in such a way that $(\sqrt{3}L_7/2L_5)^{3M} < \delta$, where δ is a positive quantity much smaller than unity. With the decrease of δ, the number of the modes included in the calculation increases.

Figure 20 shows some examples of calculated transmission and reflection probabilities for $\delta = 10^{-4}$ and 10^{-8}. As for the transmission, contributions from intervalley scattering ($K \to K'$) are plotted together for several values of θ. The dependence on the value of δ is extremely small and is not important at all, showing that the analytic expressions for the transmission and reflection probabilities obtained above are almost exact.

Explicit calculations were performed also for $\varepsilon \neq 0$ [89] and figure 21 shows an example. The conductance grows with the energy and has a peak before the first band edge $\varepsilon/\gamma = \pm 2\pi/L_5$. This behaviour arises from the oscillatory feature of the Bessel and Neumann functions, which appear in the eigenmodes in the junction region as in equation (5.3). Near the band edge, the conductance decreases abruptly and falls off to zero. This behaviour cannot be obtained if we ignore the evanescent modes in the tube region [90]. This implies the formation of a kind of resonant state in the junction region, which would bring forth the total reflection into the thicker tube region. The tight-binding results [88, 90] show a small asymmetry between $\varepsilon > 0$ and $\varepsilon < 0$. The asymmetry arises presumably from the presence of five- and seven-member rings and is expected to be reduced with the increase of the circumference length.

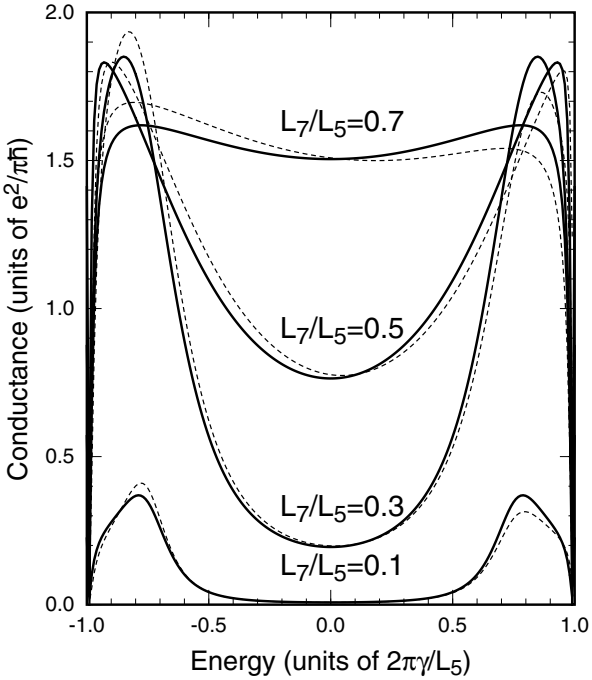

Figure 21. Calculated conductance versus the energy ε ($-2\pi/L_5 < \varepsilon/\gamma < +2\pi/L_5$) for various values of the junction length. Solid lines represent the results of the $\boldsymbol{k}\cdot\boldsymbol{p}$ method, while dashed lines show tight-binding data [88] for $L_5 = 50\sqrt{3}a$ (a is the lattice constant). The conductance grows with the energy and has a peak before the first band edge $\varepsilon/\gamma = \pm 2\pi/L_5$, followed by an abrupt fall-off. After [89].

Effects of a magnetic field perpendicular to the axis were also studied [91]. The results show a universal dependence on the field component in the direction of the pentagonal and heptagonal rings, similar to that in the case of vacancies discussed in the previous section. A bend junction was observed experimentally (see figure 16(b)) and the conductance across such a junction between a (6,6) armchair CN and a (10,0) zigzag CN was discussed [81]. As illustrated in figure 22 the bend junction is a special case of the general junction shown in figure 17.

Junctions can contain many pairs of topological defects. Effects of three pairs present between metallic (6,3) and (9,0) nanotubes were studied [70], which shows that the conductance vanishes for junctions having a threefold rotational symmetry, but remains nonzero for those without the symmetry. Effects of a Stone–Wales defect consisting of neighbouring two pentagonal and two hexagonal rings were studied and the resulting conductance was shown to be little influenced and close to the ideal value $2e^2/\pi\hbar$ near $\varepsilon = 0$ [92].

6. Nanotubes as a Tomonaga–Luttinger liquid

A metallic CN has energy bands having a linear dispersion in the vicinity of the Fermi level and therefore is expected to provide an ideal one-dimensional system where important

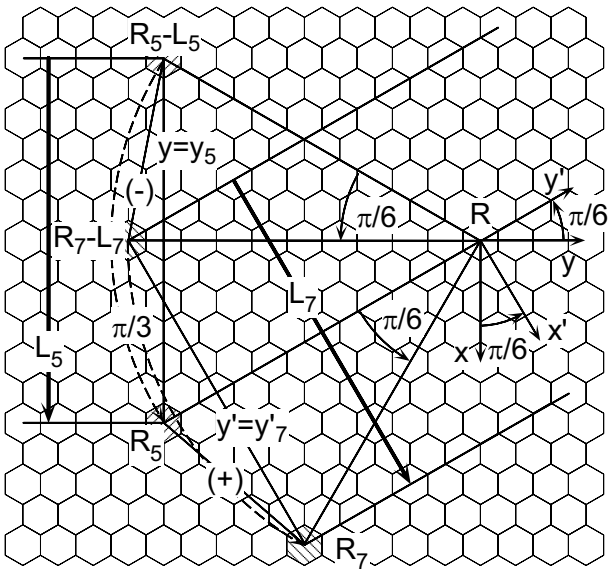

Figure 22. The structure of a bend junction consisting of a (6,6) armchair nanotube and (10,0) zigzag nanotube. It is a special case of figure 17 for $\theta = \pi/6$.

electron–electron interaction effects can be studied. In fact, there have been many theoretical works in which an effective low-energy theory was formulated and explicit predictions were made on various quantities like the energy gap at $\varepsilon = 0$, the temperature dependence of the conductivity and the tunnel conductance between the CN and a metallic contact etc [93–101]. Some experiments reported results suggesting the presence of such many-body effects [35, 36, 102].

In [102], for example, electrical connections to nanotubes were achieved by either depositing electrode metal over the top of the tubes ('end contacted') or by placing the tubes on top of predefined metal leads ('bulk contacted'). At high temperatures, the measured differential conductance exhibits a power-law dependence on temperature $\propto T^{\alpha}$ and the applied voltage $\propto V^{\alpha}$, where T is the temperature and V is the applied voltage. The obtained power α was shown to vary between two samples end and bulk contacted, in rough qualitative agreement with theoretical predictions on the exponent for tunnelling into bulk and an edge of a one-dimensional Tomonaga–Luttinger liquid.

7. Summary and conclusion

Electronic and transport properties of carbon nanotubes have been discussed theoretically based on a $\boldsymbol{k}\cdot\boldsymbol{p}$ scheme. The motion of electrons in carbon nanotubes is described by Weyl's equation for a massless neutrino with a helicity. This leads to interesting properties of nanotubes including Aharonov–Bohm effects on the bandgap, the absence of backward scattering and the conductance quantization in the presence of scatterers with a potential range larger than the lattice constant, a conductance quantization in the presence of lattice vacancies and power-law dependence of the conductance across a junction between nanotubes with different diameters.

Acknowledgments

The author acknowledges the collaboration with H Ajiki, T Seri, T Nakanishi, H Matsumura, R Saito, H Suzuura and M Igami. This work was supported in part by Grants-in-Aid for Scientific Research and Priority Area, Fullerene Network, from the Ministry of Education, Science and Culture in Japan.

References

[1] Iijima S 1991 *Nature* **354** 56
[2] Iijima S, Ichihashi T and Ando Y 1992 *Nature* **356** 776
[3] Iijima S and Ichihashi T 1993 *Nature* **363** 603
[4] Bethune D S, Kiang C H, de Vries M S, Gorman G, Savoy R, Vazquez J and Beyers R 1993 *Nature* **363** 605
[5] Hamada N, Sawada S and Oshiyama A 1992 *Phys. Rev. Lett.* **68** 1579
[6] Mintmire J W, Dunlap B I and White C T 1992 *Phys. Rev. Lett.* **68** 631
[7] Saito R, Fujita M, Dresselhaus G and Dresselhaus M S 1992 *Phys. Rev.* B **46** 1804
[8] Dresselhaus M S, Dresselhaus G and Saito R 1992 *Phys. Rev.* B **45** 6234
[9] Dresselhaus M S, Dresselhaus G, Saito R and Eklund P C 1992 *Elementary Excitations in Solids* ed J L Birman, C Sebenne and R F Wallis (Amsterdam: Elsevier) p 387
[10] Jishi R A, Dresselhaus M S and Dresselhaus G 1993 *Phys. Rev.* B **47** 16 671
[11] Tanaka K, Okahara K, Okada M and Yamabe T 1992 *Chem. Phys. Lett.* **191** 469
[12] Gao Y D and Herndon W C 1992 *Mol. Phys.* **77** 585
[13] Robertson D H, Berenner D W and Mintmire J W 1992 *Phys. Rev.* B **45** 12 592
[14] White C T, Robertson D C and Mintmire J W 1993 *Phys. Rev.* B **47** 5485
[15] Ajiki H and Ando T 1992 *J. Phys. Soc. Japan* **62** 1255
[16] Ajiki H and Ando T 1993 *J. Phys. Soc. Japan* **62** 2470 [errata *J. Phys. Soc. Japan* **63** 4267]
[17] Ajiki H and Ando T 1994 *Physica* B **201** 349
Ajiki H and Ando T 1995 *Japan. J. Appl. Phys. Suppl.* **34** 107
[18] Ajiki H and Ando T 1995 *Japan. J. Appl. Phys. Suppl.* **34** 107
[19] Ando T 1997 *J. Phys. Soc. Japan* **66** 1066
[20] Viet N A, Ajiki H and Ando T 1994 *J. Phys. Soc. Japan* **63** 3036
[21] Ajiki H and Ando T 1995 *J. Phys. Soc. Japan* **64** 260
[22] Ajiki H and Ando T 1996 *J. Phys. Soc. Japan* **65** 2976
[23] Ajiki H and Ando T 1995 *J. Phys. Soc. Japan* **64** 4382
[24] Song S N, Wang X K, Chang R P H and Ketterson J B 1994 *Phys. Rev. Lett.* **72** 697
[25] Fischer J E, Dai H, Thess A, Lee R, Hanjani N M, Dehaas D D and Smalley R E 1997 *Phys. Rev.* B **55** R4921
[26] Bockrath M, Cobden D H, McEuen P L, Chopra N G, Zettl A, Thess A and Smalley R E 1997 *Science* **275** 1922
[27] Langer L, Bayot V, Grive E, Issi J-P, Heremans J P, Olk C H, Stockman L, Van Haesendonck C and Brunseraede Y 1996 *Phys. Rev. Lett.* **76** 479
[28] Kasumov A Yu, Khodos I I, Ajayan P M and Colliex C 1996 *Europhys. Lett.* **34** 429
[29] Katayama F 1996 *Master Thesis* (University of Tokyo)
[30] Ebbesen T W, Lezec H J, Hiura H, Bennett J W, Ghaemi H F and Thio T 1996 *Nature* **382** 54
[31] Dai H, Wong E W and Lieber C M 1996 *Science* **272** 523
[32] Kasumov A Yu, Bouchiat H, Reulet B, Stephan O, Khodos I I, Gorbatov Yu B and Colliex C 1998 *Europhys. Lett.* **43** 89
[33] Tans S J, Devoret M H, Dai H-J, Thess A, Smalley R E, Geerligs L J and Dekker C 1997 *Nature* **386** 474
[34] Tans S J, Verschuren R M and Dekker C 1998 *Nature* **393** 49
[35] Cobden D H, Bockrath M, McEuen P L, Rinzler A G and Smalley R E 1998 *Phys. Rev. Lett.* **81** 681
[36] Tans S J, Devoret M H, Groeneveld R J A and Dekker C 1998 *Nature* **394** 761
[37] Bezryadin A, Verschueren A R M, Tans S J and Dekker C 1998 *Phys. Rev. Lett.* **80** 4036
[38] Dresselhaus M S, Dresselhaus G and Eklund P C 1996 *Science of Fullerenes and Carbon Nanotubes* (New York: Academic)
[39] Ebbesen T W 1996 *Phys. Today* **49** 26
[40] Ajiki H and Ando T 1997 *Solid State Commun.* **102** 135
[41] Saito R, Dresselhaus G and Dresselhaus M S 1998 *Physical Properties of Carbon Nanotubes* (London: Imperial College Press)
[42] Dekker C 1999 *Phys. Today* **52** 22
[43] Wallace P R 1947 *Phys. Rev.* **71** 622
[44] Slonczewski J C and Weiss P R 1958 *Phys. Rev.* **109** 272
[45] Tian W-D and Datta S 1994 *Phys. Rev.* B **49** 5097
[46] McClure J W 1960 *Phys. Rev.* **119** 606
[47] Soule D E, McClure J W and Smith L B 1964 *Phys. Rev.* **134** A452
[48] Ando T and Seri T 1997 *J. Phys. Soc. Japan* **66** 3558
[49] Ajiki H and Ando T 1996 *J. Phys. Soc. Japan* **65** 505
[50] Ando T and Nakanishi T 1998 *J. Phys. Soc. Japan* **67** 1704
[51] Akera H and Ando T 1991 *Phys. Rev.* B **43** 11 676
[52] Seri T and Ando T 1997 *J. Phys. Soc. Japan* **66** 169
[53] Shon N H and Ando T 1998 *J. Phys. Soc. Japan* **67** 2421
[54] Ando T, Nakanishi T and Saito R 1998 *J. Phys. Soc. Japan* **67** 2857
[55] Berry M V 1984 *Proc. R. Soc.* A **392** 45
[56] Simon B 1983 *Phys. Rev. Lett.* **51** 2167
[57] Nakanishi T and Ando T 1999 *J. Phys. Soc. Japan* **68** 561
[58] Bachtold A, Strunk C, Salvetat J P, Bonard J M, Forro L, Nussbaumer T and Schöneberger C 1999 *Nature* **397** 673
[59] Fujiwara A, Tomiyama K, Suematsu H, Yumura M and Uchida K 1999 *Phys. Rev.* B **60** 13 492
[60] McEuen P L, Bockrath M, Cobden D H, Yoon Y-G and Louie S G 1999 *Phys. Rev. Lett.* **83** 5098
[61] Frank S, Poncharal P, Wang Z L and de Heer W A 1998 *Science* **280** 1744
[62] Kane C L *et al* 1998 *Europhys. Lett.* **41** 683
[63] Suzuura H and Ando T *Mol. Cryst. Liq. Cryst.* at press
[64] Suzuura H and Ando T *Physica* E at press
[65] Zhou O, Fleming R M, Murphy D W, Haddon R C, Ramirez A P and Glarum S H 1994 *Science* **263** 1744
[66] Amelinckx S, Bernaerts D, Zhang X B, Van Tendeloo G and Van Landuyt J 1995 *Science* **267** 1334
[67] Fujita M, Wakabayashi K, Nakada K and Kusakabe K 1996 *J. Phys. Soc. Japan* **65** 1920
[68] Nakada K, Fujita M, Dresselhaus G and Dresselhaus M S 1996 *Phys. Rev.* B **54** 17 954
[69] Fujita M, Igami M and Nakada K 1997 *J. Phys. Soc. Japan* **66** 1864
[70] Chico L, Benedict L X, Louie S G and Cohen M L 1996 *Phys. Rev.* B **54** 2600
[71] Igami M, Nakanishi T and Ando T 1999 *J. Phys. Soc. Japan* **68** 716
[72] Igami M, Nakanishi T and Ando T *Mol. Cryst. Liq. Cryst.* at press
[73] Igami M, Nakanishi T and Ando T 1999 *J. Phys. Soc. Japan* **68** 3146
[74] Ando T, Nakanishi T and Igami M 1999 *J. Phys. Soc. Japan* **68** 3994
[75] Kostyrko T, Bartkowiak M and Mahan G D 1999 *Phys. Rev.* B **59** 3241
[76] White C T and Todorov T N 1998 *Nature* **393** 240
[77] Anantram M P and Govindan T R 1998 *Phys. Rev.* B **58** 4882
[78] Roche S and Saito R 1999 *Phys. Rev.* B **59** 5242
[79] Harigaya K 1999 *Phys. Rev.* B **60** 1452
[80] Kostyrko T and Bartkowiak M 1999 *Phys. Rev.* B **60** 10 735

[81] Han J, Anantram M P, Jaffe R L, Kong J and Dai H 1998 *Phys. Rev.* B **57** 14 983
[82] Chico L, Crespi V H, Benedict L, Louie S G and Cohen M L 1996 *Phys. Rev. Lett.* **76** 971
[83] Saito R, Dresselhaus G and Dresselhaus M S 1996 *Phys. Rev.* B **53** 2044
[84] Tamura R and Tsukada M 1997 *Solid State Commun.* **101** 601
[85] Tamura R and Tsukada M 1997 *Phys. Rev.* B **55** 4991
[86] Tamura R and Tsukada M 1997 *Z. Phys.* D **40** 432
[87] Matsumura H and Ando T 1998 *J. Phys. Soc. Japan* **67** 3542
[88] Nakanishi T 1997 unpublished
[89] Matsumura H and Ando T *Mol. Cryst. Liq. Cryst.* at press
[90] Tamura R and Tsukada M 1998 *Phys. Rev.* B **58** 8120
[91] Nakanishi T and Ando T 1997 *J. Phys. Soc. Japan* **66** 2973
[92] Choi H J and Ihm J 1999 *Phys. Rev.* B **59** 2267
[93] Balens L and Fisher M P A 1997 *Phys. Rev.* B **55** 11 973
[94] Krotov Yu A, Lee D-H and Louie S G 1997 *Phys. Rev. Lett.* **78** 4245
[95] Egger R and Gogolin A O 1997 *Phys. Rev. Lett.* **79** 5082
[96] Kane C, Balents L and Fisher M P A 1997 *Phys. Rev. Lett.* **79** 5086
[97] Egger R and Gogolin A O 1998 *Eur. Phys. J.* B **3** 281
[98] Lin H-H 1998 *Phys. Rev.* B **58** 4963
[99] Yoshioka H and Odintsov A A 1999 *Phys. Rev. Lett.* **82** 374
[100] Odintsov A A, Smit W and Yoshioka H 1999 *Europhys. Lett.* **45** 598
[101] Odintsov A A and Yoshioka H 1999 *Phys. Rev.* B **59** R10 457
[102] Bockrath M, Cobden D H, Jia L, Rinzler A G, Smalley R E, Balents L and McEuen P L 1999 *Nature* **397** 598